



ELSEVIER

Contents lists available at ScienceDirect

# Nuclear Instruments and Methods in Physics Research A

journal homepage: [www.elsevier.com/locate/nima](http://www.elsevier.com/locate/nima)

## Digital spectrometer for coincidence measurement of Doppler broadening of positron annihilation radiation

J. Čížek\*, M. Vlček, I. Procházka

Charles University in Prague, Faculty of Mathematics and Physics, Department of Low Temperature Physics, V Holešovičkách 2, CZ-180 00 Praha 8, Czech Republic

## ARTICLE INFO

## Article history:

Received 8 April 2010

Received in revised form

16 July 2010

Accepted 16 July 2010

Available online 12 August 2010

## Keywords:

Coincidence Doppler spectroscopy

Positron annihilation

Digitizer

Ge detector

## ABSTRACT

High-resolution digital coincidence Doppler broadening spectrometer equipped with two high-purity Ge detectors and two-channel 12-bit fast digitizer was developed and tested in this work. Two configurations were compared: (i) semi-digital setup which uses active analogue shaping of detector pulses prior to digitization to improve signal-to-noise ratio, and (ii) pure-digital setup which samples detector pulses directly. Software procedure developed for analysis of sampled waveforms, i.e. precise determination of energy of detected photon and rejection of distorted pulses, is described. Performance of digital coincidence spectrometer was compared with traditional analogue setup connected to the same detectors. It was found that digital spectrometer enables to achieve better energy resolution than in traditional analogue setup. Moreover, in digital configuration one has better control over shape of the signal. This allows efficient elimination of undesired distorted or damaged waveforms and to obtain spectrum of better clarity. The superior parameters of new digital coincidence Doppler broadening spectrometer are demonstrated by benchmark measurements of well defined Fe and Al specimens and also by the detection of rare annihilation in flight events.

© 2010 Elsevier B.V. All rights reserved.

## 1. Introduction

Measurement of Doppler broadening (DB) of annihilation radiation is an important and widely used technique of positron annihilation spectroscopy (PAS). The annihilating electron-positron pair decays usually into two annihilation photons with energy  $E_1$  and  $E_2$ . The total energy of annihilation photons is

$$E_1 + E_2 = \sqrt{m_0^2 c^4 + p_-^2 c^2} + \sqrt{m_0^2 c^4 + p_+^2 c^2} - E_B \quad (1)$$

where  $m_0 c^2$  is the rest energy of electron,  $E_B$  is the binding energy of electron, and  $p_-$ ,  $p_+$ , respectively, is the electron and positron momentum. The non-zero momentum of the annihilating electron and positron causes a Doppler shift  $\Delta E$  in energy of annihilation photons. As momentum of positrons *thermalized* in matter is very small ( $p_+ \ll p_-$ ), the Doppler shift is determined predominantly by the electron momentum. Assuming  $p_- c \ll m_0 c^2$  the energy of one annihilation photon is  $E_1 = m_0 c^2 - E_B/2 + \Delta E$ , while the energy of the second photon is  $E_2 = m_0 c^2 - E_B/2 - \Delta E$ . The Doppler shift  $\Delta E$  is then directly proportional to the longitudinal component  $p_L$  of the electron momentum along the direction of

photon emission,

$$\Delta E = \frac{p_L c}{2}. \quad (2)$$

Hence, the Doppler shift carries information about one-dimensional momentum distribution of electrons, which annihilated positrons. The coincidence Doppler broadening (CDB) spectroscopy introduced by Lynn et al. [1] is based on simultaneous precise determination of energy of *both* annihilation photons. The energies of photons emitted in an event where a thermalized positron is annihilated by electron satisfy the following relations:

$$E_1 - E_2 = 2\Delta E = p_L c \quad (3)$$

$$E_1 + E_2 = 2m_0 c^2 - E_B. \quad (4)$$

Coincidence measurement of both annihilation photons reduces background at least by three orders of magnitude and so allows observation of the high-momentum tails of annihilation peak which come from positrons annihilated by core electrons. As deep core electrons retain their atomic character and remain virtually unaffected by crystal bonding, analysis of high momentum tails enables to identify chemical elements surrounding positron annihilation site. For this reason CDB spectroscopy is widely used e.g. for identification of defects in alloys [2–5] or for characterization of very small precipitates [6,7].

\* Corresponding author. Tel.: +420 2 2191 2788; fax: +420 2 2191 2567.

E-mail addresses: [Jakub.Cizek@mff.cuni.cz](mailto:Jakub.Cizek@mff.cuni.cz), [jcizek@mbox.troja.mff.cuni.cz](mailto:jcizek@mbox.troja.mff.cuni.cz) (J. Čížek).

A CDB spectrometer usually consists of two high-purity germanium (HPGe) detectors and corresponding analogue electronics, realized by standard nuclear instrument modules (NIMs), for determination of energy and time information. The recent development of fast digitizers, together with increasing computing power of personal computers, and growing capacity of data storage media is enabling a new approach to PAS instrumentation to be implemented. This can be termed as digital PAS (DPAS). The central difference compared to traditional analogue PAS is the use of fast digitizers to sample directly detector signals in real time and store them in a computer. Analysis of sampled waveforms is then performed offline by a suitable software procedure. DPAS has several indisputable advantages compared to traditional analogue setup:

- (i) all detector signals are directly accessible for the analysis, i.e. the amount of recorded information is much higher than in analogue setup,
- (ii) data analysis can be repeated many times and one can find the optimal strategy how to derive required physical information and how to eliminate undesired distorted or damaged pulses,
- (iii) time consuming adjustment of the analog NIM devices is not necessary anymore.

In the recent years DPAS technique was successfully applied in positron-lifetime (PL) spectroscopy [8–10]. It has been demonstrated [11,12] that digital setup may improve time resolution of a PL spectrometer and efficiently suppress undesired distorted signals, which enables to obtain PL spectrum of improved clarity. However, for these advantages to be realized in practice it is crucial that the analysis software is correctly implemented [13].

One can expect that DPAS technique may improve also the performance of CDB spectrometers. CDB spectrometer consisting of HPGe detectors connected to digital signal processor (DSP) was described in Ref. [14]. In this work it was shown that replacement

of the traditional analogue spectroscopy track by DSP improves energy resolution and stability of the spectrometer. This result is promising although it has to be mentioned that sampled detector signals are not directly available for software analysis in configuration with DSP described in Ref. [14]. In the study reported here we describe new digital CDB spectrometer developed in our laboratory and also software procedure used in data analysis. Performance of the digital spectrometer is compared with traditional analogue setup connected to the same detectors. It is demonstrated that digital setup does improve energy resolution of spectrometer and quality of obtained CDB spectrum.

## 2. Experimental details

A  $^{22}\text{Na}_2\text{CO}_3$  (Ithemba Labs) with activity of  $\approx 1$  MBq deposited on a 2  $\mu\text{m}$  thick mylar foil (Dupont) was used as positron source in all measurements. A well annealed pure Al (99.99999%) and Fe (99.99%) were measured as reference samples. Positron source was always sandwiched between two identical pieces of each sample.

Digital and analogue setup were tested with identical HPGe detectors Canberra GC 3519, serial number B03101 (detector 1), and GC 3018, serial number B06036 (detector 2) with relative efficiency of 35% and 30%. The detectors are equipped with charge sensitive preamplifier Canberra 2002C with RC feedback mounted directly in the detector housing. The HPGe detectors were placed in face-to-face geometry with the positron source-sample sandwich on the central common axis of both detectors. The distance of detectors from the source was adjusted to have count rate approximately 3000 c/s in each detector in single mode (i.e. without coincidence). An auxiliary  $^{137}\text{Cs}$  radioisotope was placed beside the positron source-sample sandwich. The 662 keV line of  $^{137}\text{Cs}$  was used for better energy calibration of the spectrometer and for testing of energy resolution.

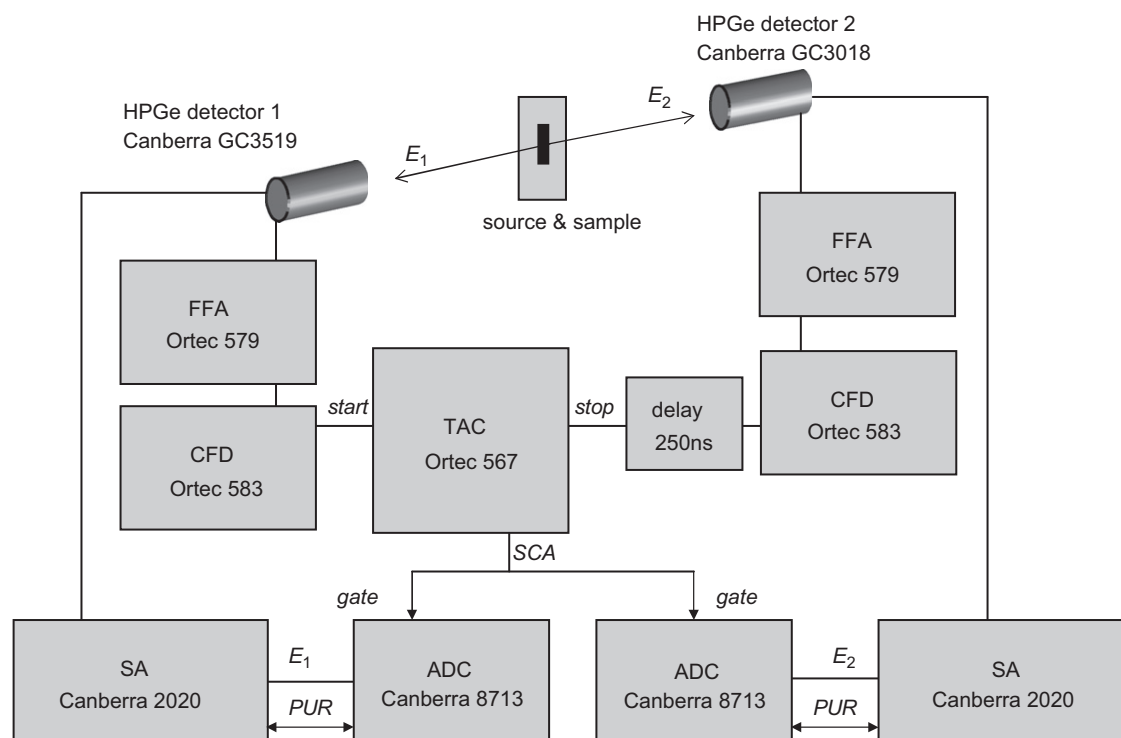


**Fig. 1.** Scheme of analogue CDB spectrometer. Meaning of the abbreviations in the figure: FFA—fast filter amplifier, CFD—constant fraction discriminator, TAC—time-to-amplitude converter, SA—spectroscopy amplifier, ADC—analogue-to-digital converter, PUR—the pile-up rejector logical signal, SCA—single channel analyzer logic output signal produced by TAC.

## 2.1. Analogue setup

Scheme of analogue CDB spectrometer is shown in Fig. 1. The spectrometer consists of two tracks: (i) energy track used for precise determination of energy of detected photons and (ii) coincidence timing track used to derive time information about detected photons. The energy track is gated by the timing circuit to ensure that only such events where photons were detected simultaneously in both detectors are accepted. The energy track consists of two spectroscopy amplifiers (SAs) Canberra 2020 used for pseudo-Gaussian shaping (time constant  $4\ \mu\text{s}$ ) and amplification of signals from preamplifier of HPGe detectors. Amplitudes of output pulses from SAs are converted by 13-bit analogue-to-digital converters (ADCs) Canberra 8713. Each SA is equipped with pile-up rejector circuit which produces logical PUR signal which disables conversion in ADC, i.e. rejects pulses damaged by pile up [15]. The timing circuit is fed by the second output of HPGe detectors and consists of fast-filter amplifiers (FFAs) Ortec 579 used for amplification and shaping of detector pulses into a form suitable for differential constant fraction discriminators (CFDs) Ortec 583. In order to reject uninteresting low energy pulses the lower level threshold of the amplitude window of CFDs was set to a level corresponding to  $\approx 250\ \text{keV}$ . No restriction was imposed on the upper level. Final determination of time interval between the detected photons is performed by time-to-amplitude converter (TAC) Ortec 567 fed by timing signals from CFDs. The conversion cycle of TAC is started by a signal from the first detector and stopped by a signal from the second detector with a constant delay of  $\approx 250\ \text{ns}$  added. The time difference required to consider the signals from both detectors as coincidence event can be conveniently adjusted by the single channel analyzer (SCA) window of TAC. The SCA slow-positive NIM logic signal produced by TAC is used to gate the ADCs. Hence data from SAs are accepted only if the event was evaluated as a coincidence by the time circuit.

The coincidence count rate achieved with 1 MBq source was approximately 500 c/s. The pairs of detected photon energies  $E_1$  and  $E_2$  were stored. Subsequently, a two-dimensional histogram of  $E_1 + E_2 - 2m_0c^2$  versus  $E_1 - E_2$  was constructed from these data.

## 2.2. Digital setup

Fast digitizer is the main part of any digital spectrometer. The digital CDB spectrometer described here is equipped with a two-channel 12-bit digitizer Agilent Technologies U1066A (Acqiris DC 440) which enables sampling of detector signals with frequency up to 420 MHz. Hence, signals from the first detector are led to channel 1, and signals from the second detector to channel 2, of the digitizer. Typical shape of detector pulse produced by annihilation photon is shown in Fig. 2a. As the rise time of detector pulse is  $\approx 300\ \text{ns}$ , the sampling rate of 420 MHz is fast enough for proper sampling of detector signals. Each detector pulse is followed by an exponential tail with decay constant of  $\approx 50\ \mu\text{s}$  produced by discharging of the feedback capacitor. As precise determination of energy of annihilation photons is very important in CDB spectroscopy, the vertical resolution of digitizer should be high enough. The amplitude of detector pulses produced by the annihilation photons is  $\sim 90\ \text{mV}$ , approximately a third of the most sensitive range of digitizer Acqiris DC 440 with full scale of 250 mV. Hence, full scale of the digitizer in the most sensitive range corresponds to the energy of  $\approx 1400\ \text{keV}$ . The bin width of the digitizer is  $\Delta_b = 1400/2^{12} \approx 0.34\ \text{keV}$ . Assuming uniform distribution within each bin the uncertainty (standard deviation) in energy caused by finite bin size is  $\sigma_b = \Delta_b/\sqrt{12} \approx 0.1\ \text{keV}$ . This value corresponds to the full width at half maximum (FWHM)  $w_b = 0.2\ \text{keV}$ . Such uncertainty caused

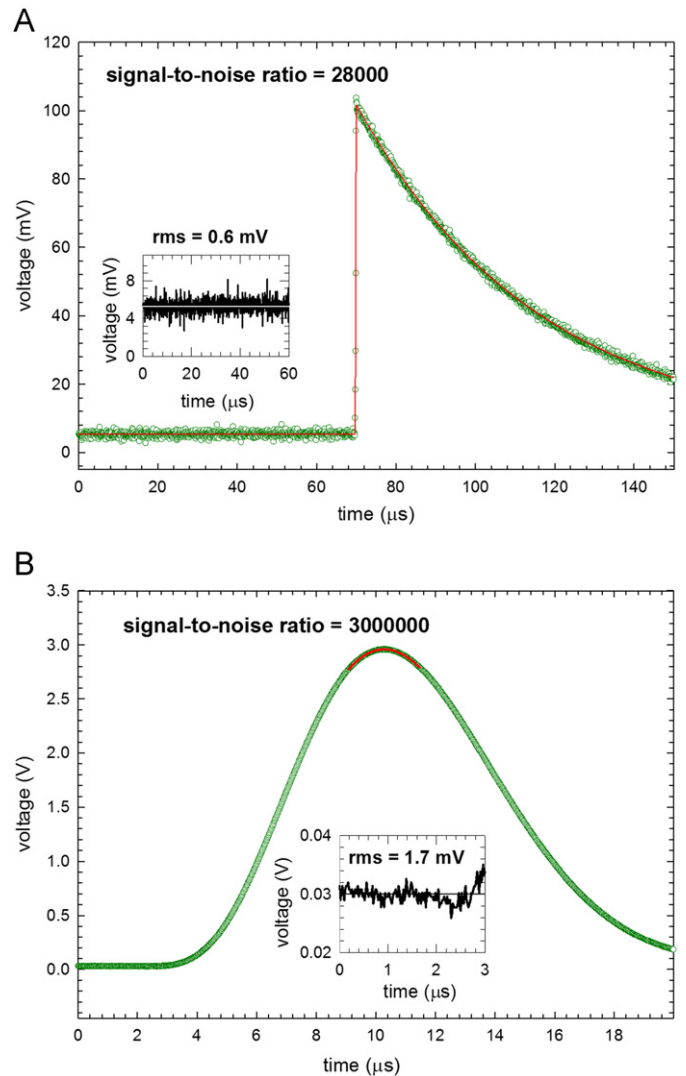


**Fig. 2.** Typical shape of signal produced by 511 keV annihilation photon: (A) signal taken directly from detector pre-amplifier; solid line shows fit of the signal by model function given by Eq. (5); (B) pseudo-Gaussian pulse shaped by spectroscopy amplifier (timing constant  $4\ \mu\text{s}$ ); solid line shows parabolic fit of pulse maximum. The insets present zoomed base-line part of the signal preceding the pulse and estimated rms value.

by finite bin width is acceptable. For example if FWHM of certain energy peak is  $w_0 = 1.20\ \text{keV}$  that it would be broadened due to finite bin size to  $\sqrt{w_0^2 + w_b^2} = 1.22\ \text{keV}$ .

In the traditional analogue setup the detector pulses are modified by SA using active CR high-pass and RC low-pass frequency filters. Detector pulses are not only amplified but also shaped, i.e. their overall width is sharpened and the high frequency noise is smoothed. In the frequency domain this corresponds to the suppression of the very high and low frequency components. Hence, shaping of detector signals by SA improves significantly signal-to-noise ratio of detector pulses. Fig. 2A shows typical detector pulse (i.e. signal taken directly from detector pre-amplifier) produced by 511 keV photon, while Fig. 2B shows such pulse amplified and shaped by SA. Insets in Fig. 2 show zoomed base-line preceding the pulse and estimated rms value of the base-line noise. The signal-to-noise ratio of  $\sim 28,000$  was estimated for the 511 keV photon pulse taken directly from detector preamplifier, see Fig. 2A. The signal-to-noise ratio of the same pulse modified by SA, see Fig. 2B, is  $\sim 3,000,000$ , i.e. it was increased by two orders of magnitude.

In this work we compared two digital configurations of CDB spectrometer:

- (i) Semi-digital setup with analogue shaping of detector signals. This configuration is shown in Fig. 3. Detector pulses are first amplified and shaped by SA Canberra 2020 with timing constant of 4 μs in order to improve signal-to-noise ratio. Pseudo-Gaussian output SA pulses are then sampled by digitizer. Fig. 2B shows such a pulse.
- (ii) Pure-digital setup which uses directly sampled detector signals without any analogue shaping. Scheme of this

configuration is depicted in Fig. 4. The output pulses from detector pre-amplifiers (see Fig. 2A) are directly led to digitizer inputs and are sampled.

Obviously, the advantage of the semi-digital setup is significantly improved signal-to-noise ratio of sampled pulses. A disadvantage of this configuration is a necessity of additional analogue NIM modules (two SAs) and also additional noise produced by the amplifier which is added to the detector signal. The signals could also be negatively influenced by possible non-linearities of SA.

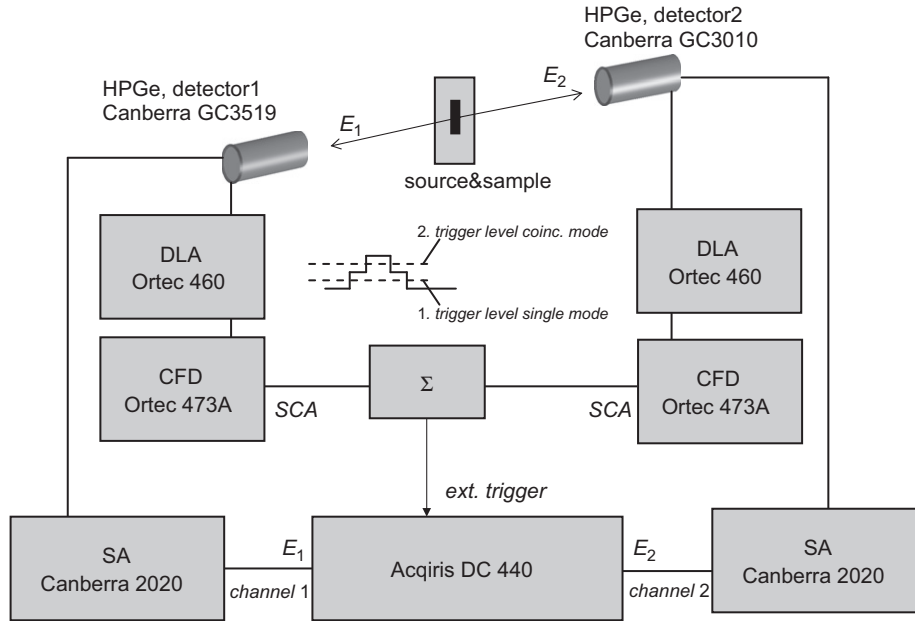


Fig. 3. Scheme of digital CDB spectrometer which uses detector pulses shaped by spectroscopy amplifier. Meaning of the abbreviations in the figure: DLA—delay line amplifier, CFD—constant fraction discriminator,  $\Sigma$ —impedance matched passive summing circuit, SA—spectroscopy amplifier.

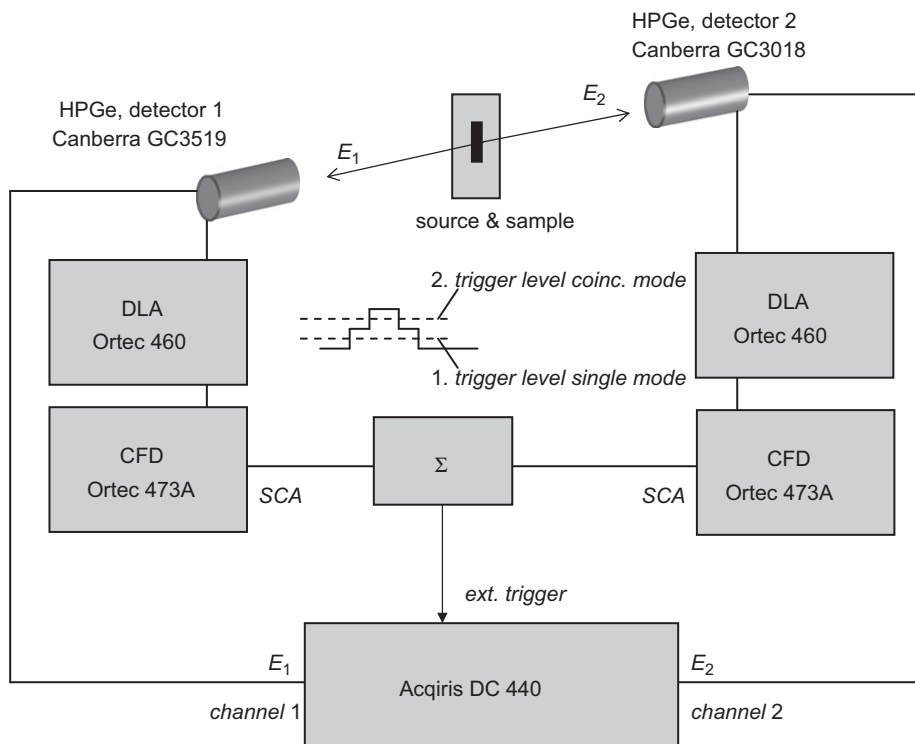


Fig. 4. Scheme of digital CDB spectrometer which uses directly detector pulses. Meaning of abbreviations is the same as in Fig. 3.

The digitizer is externally triggered by the timing circuit in both digital configurations. This consists of two CFDs fed by the detector signals amplified and shaped by delay line amplifiers (DLAs) Ortec 460. The timing SCA slow-positive NIM logic signals produced by CFDs are added by a simple impedance matched passive summing circuit ( $\Sigma$ ) and used as external trigger signal for the digitizer. As shown schematically in Figs. 3 and 4 one can select two modes of measurement by setting the trigger level of digitizer:

- (i) *single mode*, trigger level (position 1)—a photon detected in any detector starts sampling and data acquisition;
- (ii) *coincidence mode*, trigger level (position 2) set so that it can be exceeded only by a sum of the CFDs SCA signals; hence, only two photons detected simultaneously in both detectors can start sampling and data acquisition.

The trigger level of digitizer may be adjusted at any time during measurement by a simple software command. It should be mentioned that the timing circuit is used only as a gate to ensure that only coincidence events are recorded in the *coincidence mode*. The actual time difference between the signals from both detectors is determined off-line by software.

Measurement in digital configuration was performed in separate sessions. Each session consists of two parts: (i) 50,000 events accumulated in the single mode to obtain single spectra for precise energy calibration, (ii) 100,000 events accumulated in the coincidence mode. Energy calibration is performed independently for each session using the positions of annihilation peak (511 keV), auxiliary  $^{137}\text{Cs}$  source (662 keV), and  $^{22}\text{Na}$  start photon (1274 keV) determined in the spectrum measured in single mode. Measurement with analogue setup was performed also in sessions, however, without switching between the single and the coincidence mode. Independent energy calibration for each session allows possible drift of SA gain and/or walk of base-line to be compensated.

### 2.3. Data analysis

#### 2.3.1. Analogue setup

Raw data, i.e. pairs of values produced by ADCs and proportional to energies  $E_{1,2}$  of photon detected in the first and the second detector, were stored in personal computer during measurement. Energy calibration and construction of two-dimensional CDB spectrum, i.e. histogram of  $E_1 + E_2 - 2m_0c^2$  sum versus  $E_1 - E_2$ , was performed off-line in software.

#### 2.3.2. Semi-digital setup

Fig. 2B shows typical sampled waveform measured in a semi-digital configuration. The waveform consists of 1000 points with a sampling period of 20 ns. The analysis of sampled waveforms is performed in a sequence of two runs. The operations performed in the first run (run 1) can be summarized as follows:

##### run 1 (single mode):

1. Read waveform.
2. Determine maximum of the waveform by parabolic fitting, see Fig. 2B.
3. Determine the onset of the pulse and fit the base-line level prior to the pulse by a constant line. The onset of the pulse is determined as the point where derivative of the waveform crossed a preselected threshold level.
4. Apply the fixed filters. These filters are watchdogs used for a raw selection of waveforms in order to reject seriously damaged pulses from

further processing. The fixed filters also eliminate waveforms with maxima that fall outside a relatively wide energy window (corresponding to  $\sim 350$  to  $\sim 1500$  keV). In addition, fixed filters check rms of base-line and  $\chi^2$  value for the parabolic fit of pulse maximum. Waveform is rejected if rms or  $\chi^2$  values exceed a preselected level. The waveform is accepted for further processing only if it passed all fixed filters.

5. Calculate pulse height as a difference between the pulse maximum obtained by parabolic fitting and the base-line level and add the height to a histogram.
6. Normalize the waveform to a common height and shift it along the horizontal scale to set position of its maximum to a common reference time.
7. Add normalized waveform to a histogram of pulse shapes.

These operations are performed on the waveforms measured in the single mode in each session. The run 1 creates a histogram of pulse heights, which is subsequently calibrated using known energies of the annihilation peak (511 keV), auxiliary  $^{137}\text{Cs}$  radioisotope (662 keV), and  $^{22}\text{Na}$  start photon (1274 keV). The energy calibration is performed independently for each session in order to compensate possible drift of base-line level or gain of detector preamplifier and/or SA. Fig. 5 shows the total energy spectrum, i.e. summed partial spectra from all sessions, for reference Al specimen. The calibration created in run 1 is used subsequently in run 2 to calibrate the spectra measured in coincidence mode. Single mode spectra are very suitable for precise energy calibration because a sufficient statistics of all peaks used in calibration (including single photon peaks 662 and 1274 keV) can be obtained in a short time.

Fig. 6A shows an example of a randomly selected 1000 “raw” waveforms, i.e. waveforms which passed fixed filters. The same waveforms normalized to the same amplitude and with their maxima shifted to a common reference time are plotted in Fig. 6B.

A two-dimensional histogram of shapes of normalized waveforms shifted to a common reference time is created in run 1 for each detector. Such histogram shown in Fig. 7 is used to determine “ideal shape” of waveform which is constructed by connecting the most frequently occurred values for each time point (horizontal channel), i.e. modes of one-dimensional distributions representing vertical cuts of the two-dimensional

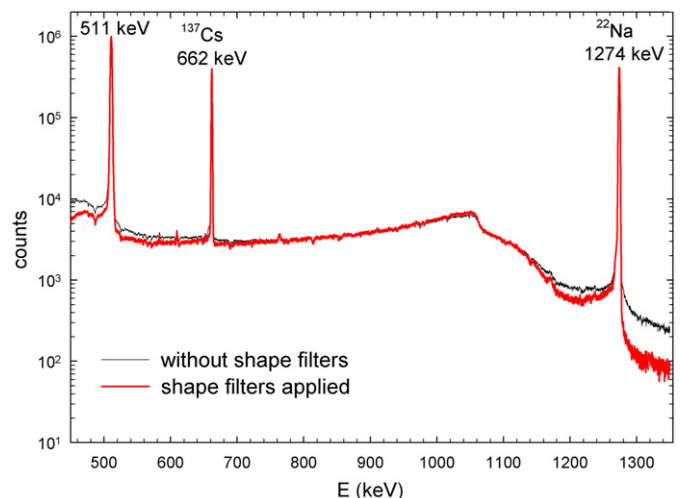
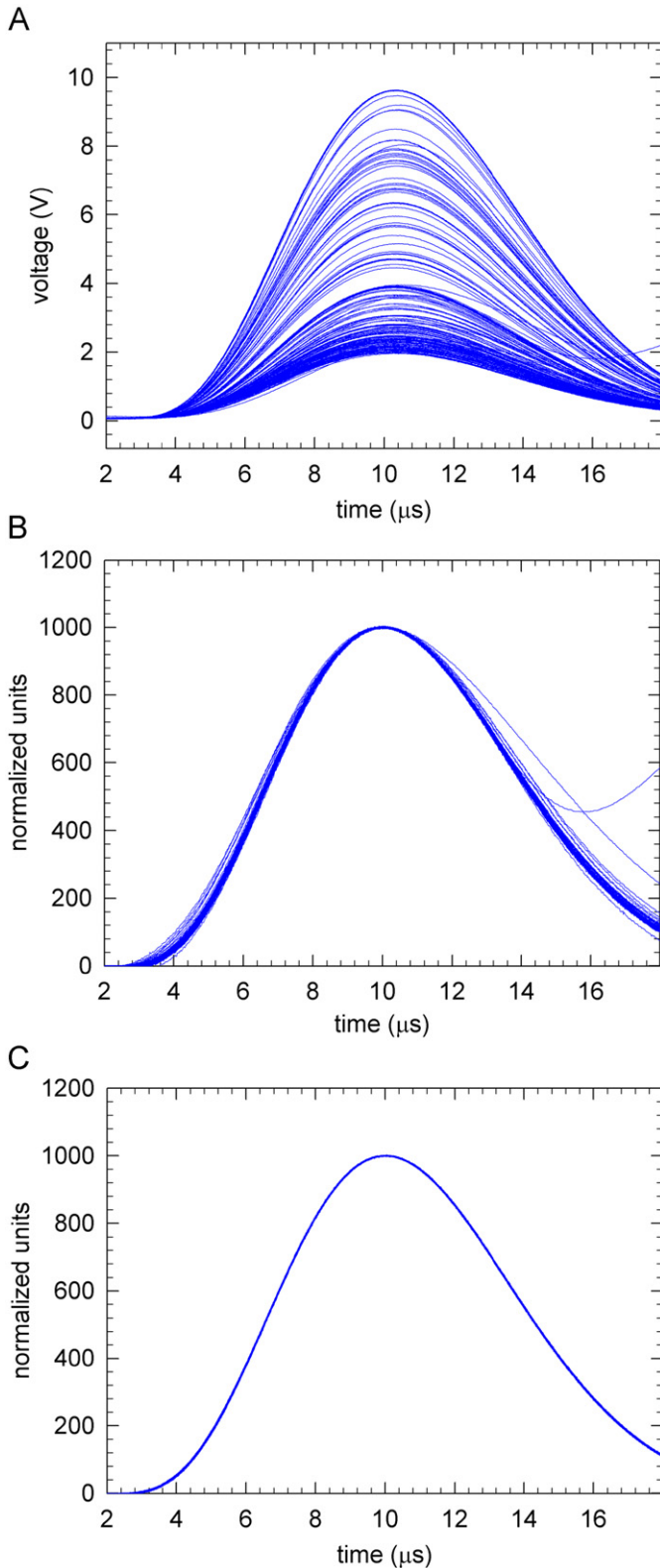
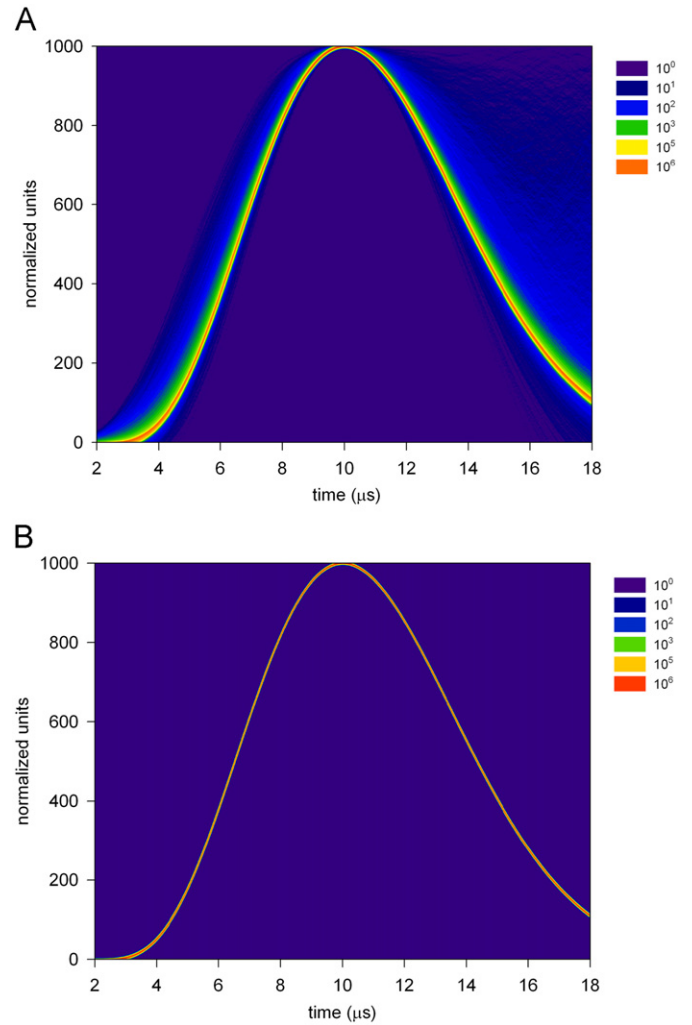


Fig. 5. Single energy spectrum constructed from waveforms measured in the semi-digital configuration in the single mode by detector 1. The spectrum obtained without application of shape filters, i.e. constructed from all waveforms accepted by fixed filters, is plotted by a thin line, while the spectrum constructed only from waveforms accepted by shape filters is plotted by a thick line. Both spectra are normalized to a common height of the annihilation peak at 511 keV.



**Fig. 6.** Example of waveforms measured by detector 1 in the single mode (A) randomly selected 1000 waveforms which passed fixed filters, (B) normalized waveforms shifted to common reference time, (C) normalized waveforms which passed shape filters.

histogram in Fig. 7. An example of such one-dimensional distribution obtained as vertical cut from the two-dimensional histogram is plotted in Fig. 8. The “ideal waveform shape” determined by this procedure for detector 1 is plotted in Fig. 9.



**Fig. 7.** Two-dimensional histogram of shapes of normalized waveforms measured by detector 1 shifted to a common reference time. (A) Histogram constructed from all waveforms which passed fixed filters, (B) only waveforms accepted by shape filters.

The energy calibration and the “ideal shape” of waveform are used in the run 2 for analysis of data measured in the coincidence mode and can be schematically described by the following sequence:

**run 2 (coincidence mode):**

1. Read waveform.
2. Determine maximum of the waveform by parabolic fitting, see Fig. 2B.
3. Determine the base-line.
4. Apply the fixed filters. The waveform is accepted only if it passed the fixed filters.
5. Normalize waveform and shift it on the horizontal scale to set position of its maximum to the common reference time. The operations 1–5 are the same as in run 1.
6. Apply the shape filter.

This filter compares shape of the normalized waveform shifted to the common reference time with the “ideal waveform shape”. The waveform is accepted only if it everywhere falls within a certain band around the “ideal shape”. This band is defined by upper and lower limits at positions where distribution in each time channel falls to  $\frac{1}{10}$  of its maxima. This procedure is illustrated in Fig. 8 which shows an example of distribution in one time channel and

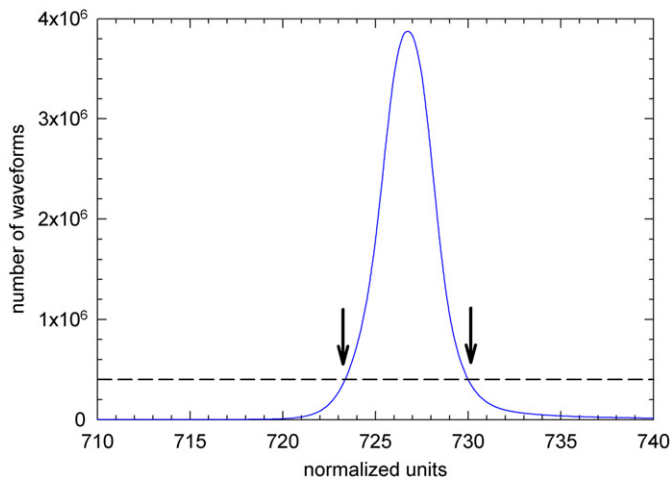


**Fig. 8.** An example of one-dimensional distribution of shapes of normalized waveforms in one time channel (i.e. a vertical cut of two-dimensional histogram in Fig. 7A) and schematic description of determination of the band width of shape filter in this time channel. The dotted line shows the level corresponding to  $\frac{1}{10}$  of maximum of the distribution. The lower and upper limits of chosen shape filter band are indicated by arrows.

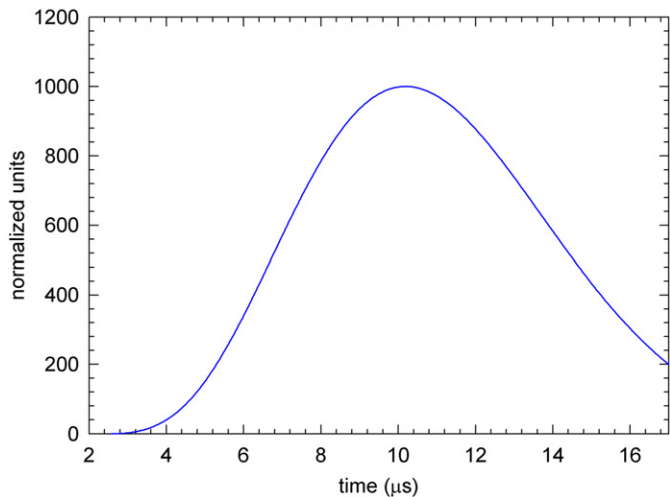


**Fig. 9.** Ideal waveform shape for detector 1 obtained from two-dimensional histogram in Fig. 7.

determination of band width in this channel. Fig. 6C shows only those normalized waveforms from Fig. 6B which were accepted by shape filters.

7. Calculate pulse height as a difference between the pulse maximum obtained by parabolic fitting and the base-line. Using known calibration convert heights to energies and add the energy to histogram.
8. Determine time interval between maxima of waveform detected in the first and second detector. The waveforms are accepted only if the time interval between them is smaller than preselected value of 200 ns.
9. Construct two-dimensional histogram of  $E_1 + E_2 - 2m_0c^2$  keV versus  $E_1 - E_2$ .
10. Calculate one-dimensional cuts of the two-dimensional histogram.

### 2.3.3. Pure digital setup

A typical sampled waveform from detector preamplifier is shown in Fig. 2A. The waveform which consists of 2500 points

with sampling period of 60 ns was fitted by a model function

$$f(t) = f_{main}(t-t_0) + f_{prec}(t) + bcg \quad (5)$$

consisting of the main pulse

$$f_{main}(t) = \left[ \frac{1}{\beta_2 \sqrt{2\pi}} \exp\left(-\frac{t^2}{2\beta_2^2}\right) \right] * [\beta_0 H_s(t-t_0) \exp(-\beta_1(t-t_0))] \quad (6)$$

approximated by an exponential decay function originated at time  $t_0$  and characterized by a decay rate  $\beta_1$  and amplitude  $\beta_0$ . The exponential decay function is multiplied by the Heaviside step function  $H_s$  and the product is convoluted (the symbol  $*$  denotes convolution) with a Gaussian with standard deviation  $\beta_2$  representing finite resolution of detector. Exponential tail of a pulse which may precede the main pulse is approximated by an exponential decay

$$f_{prec}(t) = \beta_3 \exp(-\beta_1 t) \quad (7)$$

with decay rate  $\beta_1$  and amplitude  $\beta_3$ . The base-line is modeled by a constant level  $bcg$ . Hence, the parameter  $\beta_0$  (amplitude of the main pulse) is directly proportional to the energy of detected photon.

Damaged pulses were rejected using standard  $\chi^2$  test. The sampled waveforms are analyzed again in two sequential runs. The operations performed during the first run can be summarized as follows:

#### run 1 (single mode):

1. Read waveform.
2. Fit waveform by the model function (5).
3. Calculate  $\chi^2$  value. Accept the waveform only if  $\chi^2$  per degree of freedom is smaller than a preselected value 1.07 corresponding to the significance level 0.01.
4. Add the main pulse amplitude  $\beta_0$  to histogram.

Histogram of pulse amplitudes was created for each session and calibrated using the known energy of annihilation peak (511 keV) and  $^{22}\text{Na}$  start photon (1274 keV). The calibration was performed independently for each session and was used in analysis of data measured in the coincidence mode. The waveforms sampled in the coincidence mode are worked out in the second run

#### run 2 (coincidence mode):

1. Read waveform.
2. Fit waveform by the model function (5).
3. Calculate  $\chi^2$  value. Accept the waveform only if  $\chi^2$  per degree of freedom is smaller than a preselected value 1.07 corresponding to the significance level 0.01. Hence the steps 1–3 are identical as in run 1.
4. Calibrate the main pulse amplitude  $\beta_0$  using the calibration determined previously in run 1.
5. Determine time interval between waveform detected in the first and second detector. The waveforms are accepted only if the time interval between them is smaller than preselected value of 200 ns.
6. Construct two-dimensional histogram of  $E_1 + E_2 - 2m_0c^2$  keV versus  $E_1 - E_2$ .
7. Calculate one-dimensional cuts of the two-dimensional histogram.

## 3. Results and discussion

### 3.1. Single mode

The single energy spectrum measured with detector 1 in the semi-digital setup is plotted in Fig. 5. The spectrum shows

Doppler broadened annihilation peak at energy of 511 keV, photo peak at energy of 662 keV originating from  $^{137}\text{Cs}$  auxiliary source, and photo peak at energy of 1274 keV which comes from the so-called start photons emitted by  $^{22}\text{Na}$  positron source. The effect of shape filters on energy spectrum can be seen in the figure from comparison of “raw” spectrum (i.e. spectrum constructed from all waveforms which passed fixed filters) and spectrum constructed only from waveforms which were accepted by shape filters. Clearly, application of shape filters leads to a reduction of background on the left side of photo peaks (due to suppression of waveforms distorted by ballistic deficit) and also on the right side of photo peaks (due to rejection of waveforms damaged by pile-ups). Very similar spectrum was obtained also in the other tested configurations. A detail of Doppler broadened annihilation peak (normalized to a common amplitude) measured in analogue setup and both digital configurations on the reference Al sample is shown in Fig. 10. One can see in the figure that both digital configurations enable to achieve improved peak-to-background ratio which is obviously due to better control over shape of detector signal and more efficient elimination of damaged or distorted signals. The effect of shape filter used in the semi-digital setup is illustrated in Fig. 11 which compares the annihilation peak in single energy spectrum constructed with and without application of shape filter. Clearly the application of shape filter suppresses background and improves the peak-to-background ratio due to efficient suppression of distorted pulses.

For an ideal detector (no surface currents, no charge losses) the width  $w$  (FWHM) of a  $\gamma$  line is

$$w = \sqrt{w_{stat}^2 + w_{preamp}^2} \quad (8)$$

where  $w_{stat}$  represents a contribution of statistical fluctuations and  $w_{preamp}$  is a noise contribution of the preamplifier. The statistical fluctuations are given by [16]

$$w_{stat} = 2.35 \sqrt{F \epsilon_p E} \quad (9)$$

where  $E$  is the photon energy,  $\epsilon_p = 2.96 \text{ eV}$  is the electron–hole pair creation energy in Ge [16], and  $F$  is the Fano factor [17]. The contribution to FWHM due to noise of the preamplifier can be estimated as [18]

$$w_{preamp} = 0.6 \text{ keV} + (10 \text{ eV/pF}) C_d \quad (10)$$

where  $C_d$  is the capacitance of detector (here  $C_d = 50 \text{ pF}$ ).

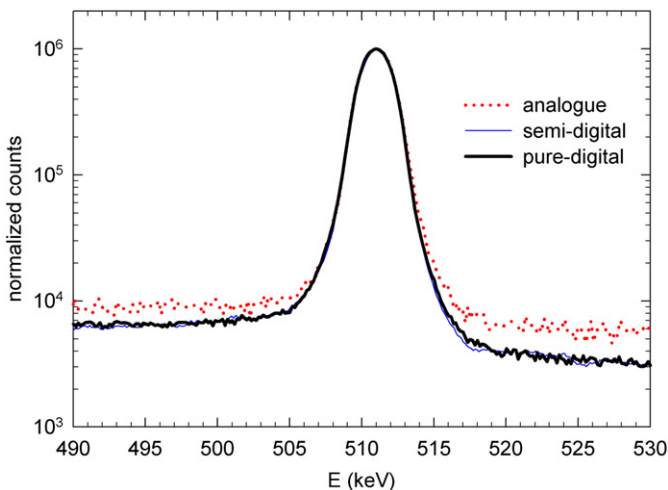


Fig. 10. A detail of the annihilation peak measured on the reference Al sample using the analogue setup and both digital configurations. The peaks were normalized to the same amplitude.

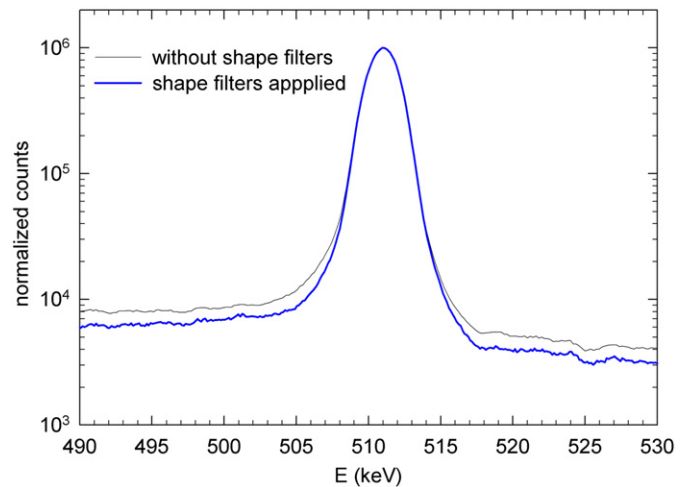


Fig. 11. A detail of the annihilation peak measured in a semi-digital setup on the reference Al sample without application of shape filter (thin line) and with shape filter (thick line). The peaks were normalized to the same amplitude.

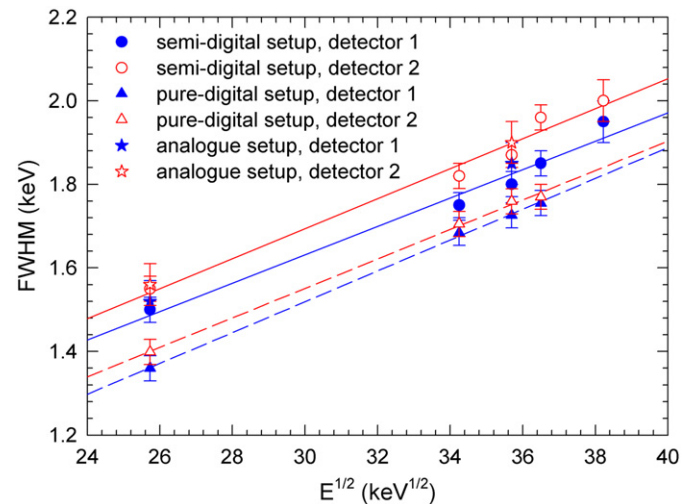


Fig. 12. FWHM of photo peaks measured in single mode in the tested configurations. FWHM of photo peaks was measured for the  $^{137}\text{Cs}$  radioisotope (662 keV), the start photon emitted by  $^{22}\text{Na}$  positron source (1274 keV). In digital configurations the energy resolution was determined also for  $^{60}\text{Co}$  (1173 keV, 1332 keV), and  $^{40}\text{K}$  (1461 keV) radioisotopes. The solid lines show linear fit by Eq. (12).

Energy resolution (FWHM of photo peaks) for both detectors is plotted in Fig. 12 as a function of the square root of energy. The solid lines in the figure show fit to the experimental points by Eq. (8). One can see in the figure that experimental points can be well approximated by linear dependence on  $\sqrt{E}$  assumed by Eq. (9). The detector 1 (GC3519) exhibits slightly better energy resolution compared to the detector 2 (GC3018). The fano factor  $F = 0.080 \pm 0.005$  was obtained from fitting for both detectors. The energy resolution obtained in a semi-digital configuration is comparable with the resolution in the analogue setup. In pure-digital configuration the energy resolution is improved roughly by 10%, see Fig. 12. The energy resolution at 511 keV estimated from the linear fit in Fig. 12 is shown in Table 1.

### 3.2. Coincidence mode

The two-dimensional histograms  $E_1 + E_2 - 2m_0c^2$  versus  $E_1 - E_2$  constructed from data measured on the reference Al sample are

plotted in Fig. 13. One can see in the figures that shape of two-dimensional histograms is very similar in all tested configurations. However, clarity of spectra measured in both digital configurations is better compared to spectrum measured in analogue setup. This is demonstrated especially by reduced background from random coincidences and suppressed “wings” above the annihilation peak due to efficient elimination of pile-ups. The one-dimensional vertical ( $E_1 - E_2 = 0$ ) and horizontal ( $E_1 + E_2 - 2m_0c^2 = 0$ ) cuts of the two-dimensional histogram represent the resolution function of CDB spectrometer and the Doppler broadened annihilation profile. These one-dimensional cuts obtained using a band with width of  $\pm 2$  keV are plotted in Fig. 14. Doppler broadened profiles obtained in all tested configurations are obviously very similar. On the other hand, shape of the resolution function differs in the tested configurations. The energy resolution of CDB spectrometer,  $w_{CDB}$  i.e. FWHM associated with the uncertainty of measured Doppler shift  $\Delta E$ , can be deduced from FWHM of the resolution function  $w_{RF}$ , see Fig. 14. As  $E_1 - E_2$  gives two times the Doppler shift, see Eq. (3), the energy resolution of a CDB spectrometer can be expressed as

$$w_{CDB} = \frac{w_{RF}}{2}. \quad (11)$$

The energy resolution determined from FWHM of the resolution function for various configurations is shown in Table 1.

Alternatively one can estimate resolution of CDB spectrometer also from known energy resolution of HPGe detectors determined in the single mode, see Fig. 12:

$$w_{CDB} = \frac{1}{2} \sqrt{(w_{1,511}^2 + w_{2,511}^2)} \quad (12)$$

where  $w_{1,511}$ ,  $w_{2,511}$  is the energy resolution of HPGe detectors 1 and 2 at energy of 511 keV. The resolutions  $w_{1,511}$ ,  $w_{2,511}$  were obtained by extrapolation of the dependence shown in Fig. 12. The resolution  $w_{CDB}$  estimated by using Eq. (12) is shown also in Table 1. Clearly, the resolution obtained by using Eq. (11) agrees well with that estimated by using Eq. (12). The energy resolutions achieved in analogue and semi-digital configurations are comparable. The best energy resolution of  $\approx 0.9$  keV was achieved in the pure digital setup. This confirms the result obtained in the single mode that fitting of the sampled detector pulses is a more precise way of how to determine energy of detected photons because contrary to analogue and semi-digital setup the signal is not influenced by additional noise created in the amplifier.

Moreover, one can see in Fig. 14 that resolution functions obtained in both digital configurations exhibit improved peak-to-background ratio compared to analogue setup. This testifies that in digital setup one has better control over the signal shapes and can more efficiently eliminate “bad” pulses damaged by pile-up effect with another photon or distorted due to ballistic deficit during charge collection. The effect of digital filtering (i.e. application of

**Table 1**

Energy resolution (in keV) at energy of 511 keV achieved in the tested configurations.

Configuration	Single mode		Coincidence mode	
	Det. 1	Det. 2	Both detectors	
	Canberra GC3519	Canberra GC3018	$w_{CDB}$ Eq. (11)	$w_{CDB}$ Eq. (12)
Analogue	$1.40 \pm 0.05$	$1.43 \pm 0.05$	$1.00 \pm 0.04$	$0.99 \pm 0.02$
Semi-digital	$1.38 \pm 0.03$	$1.43 \pm 0.03$	$0.99 \pm 0.02$	$0.99 \pm 0.02$
Pure-digital	$1.21 \pm 0.03$	$1.29 \pm 0.03$	$0.88 \pm 0.02$	$0.89 \pm 0.02$

The energy resolution in single mode was estimated from linear fit in Fig. 12. The resolution in coincidence mode was calculated from Eqs. (11) and (12).

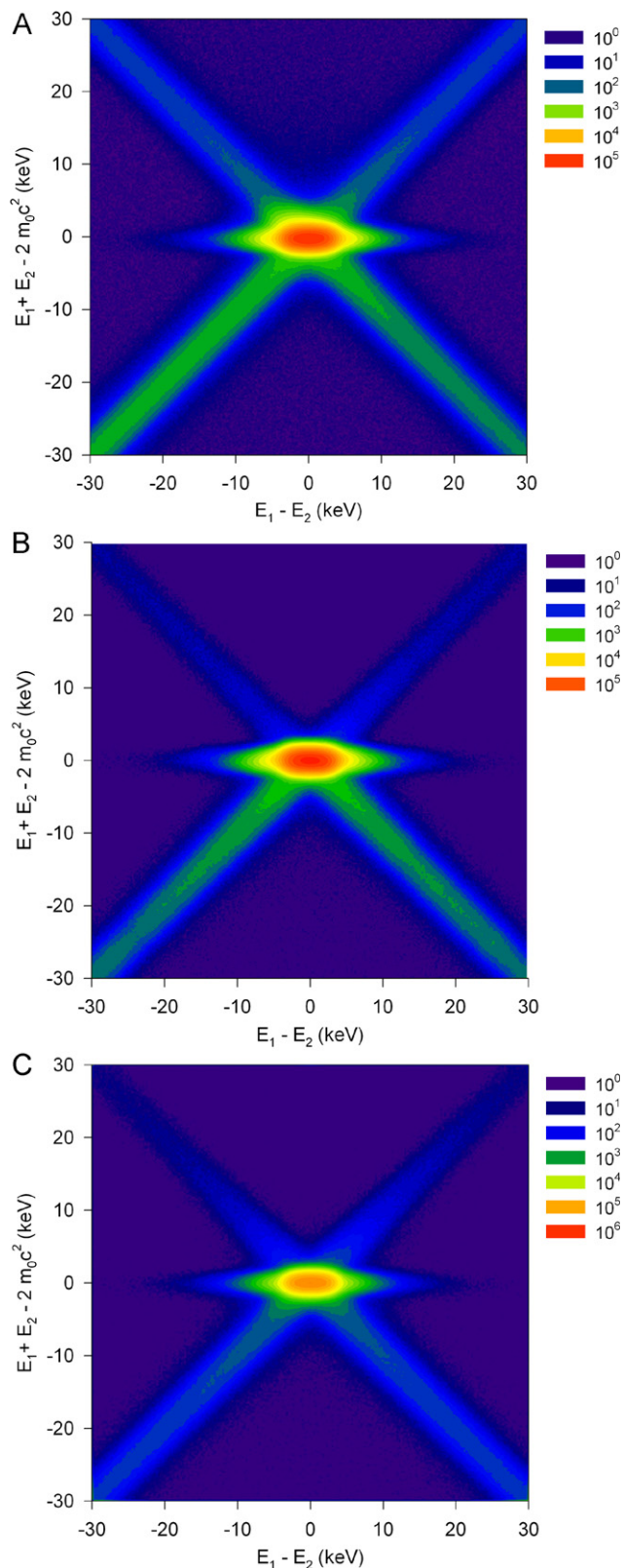


**Fig. 13.** The two-dimensional CDB spectra, i.e. histogram  $E_1 + E_2 - 2m_0c^2$  versus  $E_1 - E_2$ , measured on pure Al reference sample by means of (A) analogue setup, (B) semi-digital setup, and (C) pure-digital setup.

shape filters in semi-digital setup and  $\chi^2$  test in the pure digital configuration) on resolution function is demonstrated in Fig. 15. Without application of shape filters (i.e. all waveforms which passed fixed filters are accepted) the peak-to-background ratio of

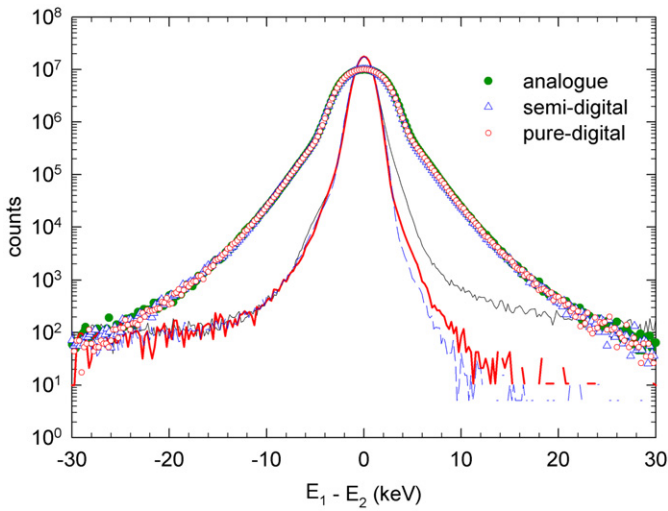


**Fig. 14.** One-dimensional cuts of CDB spectra corresponding to the Doppler broadened profile (points) and resolution function (lines). One-dimensional cuts measured in analogue (full circles, thin solid line), semi-digital (open triangles, dashed line) and pure-digital (open circles, thick solid line) configuration are compared. The spectra were measured on pure Al reference sample. The cuts obtained in various configurations were normalized to the same amplitude.

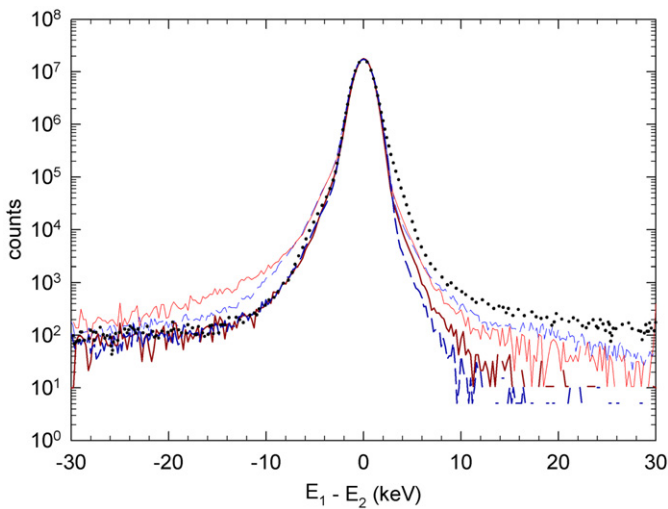


**Fig. 15.** Resolution function measured in semi-digital (dashed lines) and pure-digital (solid lines) configurations. The resolution functions obtained in both digital configurations with (thick lines) and without (thin lines) application of shape filters are compared. Resolution function obtained in the analogue setup is plotted in the figure by dotted line for comparison.

resolution function in both digital configurations is comparable to that achieved in analogue setup. However, application of filters causes suppression of background and a noticeable improvement of peak-to-background ratio. The background on the right side of the resolution function is suppressed roughly by one order of magnitude, see Fig. 15 due to elimination of waveforms damaged by pile-ups. Application of shape filters reduces also tails on the left side of resolution function, see Fig. 15. This is due to rejection of improper waveforms distorted due to ballistic deficit.

Hence, shape filtering in digital configurations rejects the undesired waveforms with distorted shape. Fig. 16 shows the effect of shape filtering on two-dimensional CDB spectrum (i.e. two-dimensional histogram  $E_1 + E_2 - 2m_0c^2$  versus  $E_1 - E_2$ ) measured in a semi-digital setup. The spectrum constructed from all waveforms which passed the fixed filters (i.e. no shape filtering applied) is plotted in Fig. 16A, while Fig. 16B shows the CDB

spectrum constructed only from waveforms which passed the shape filters. The relative differences between the spectra shown in Figs. 16A and B are plotted in Fig. 16C. One can see in the figure

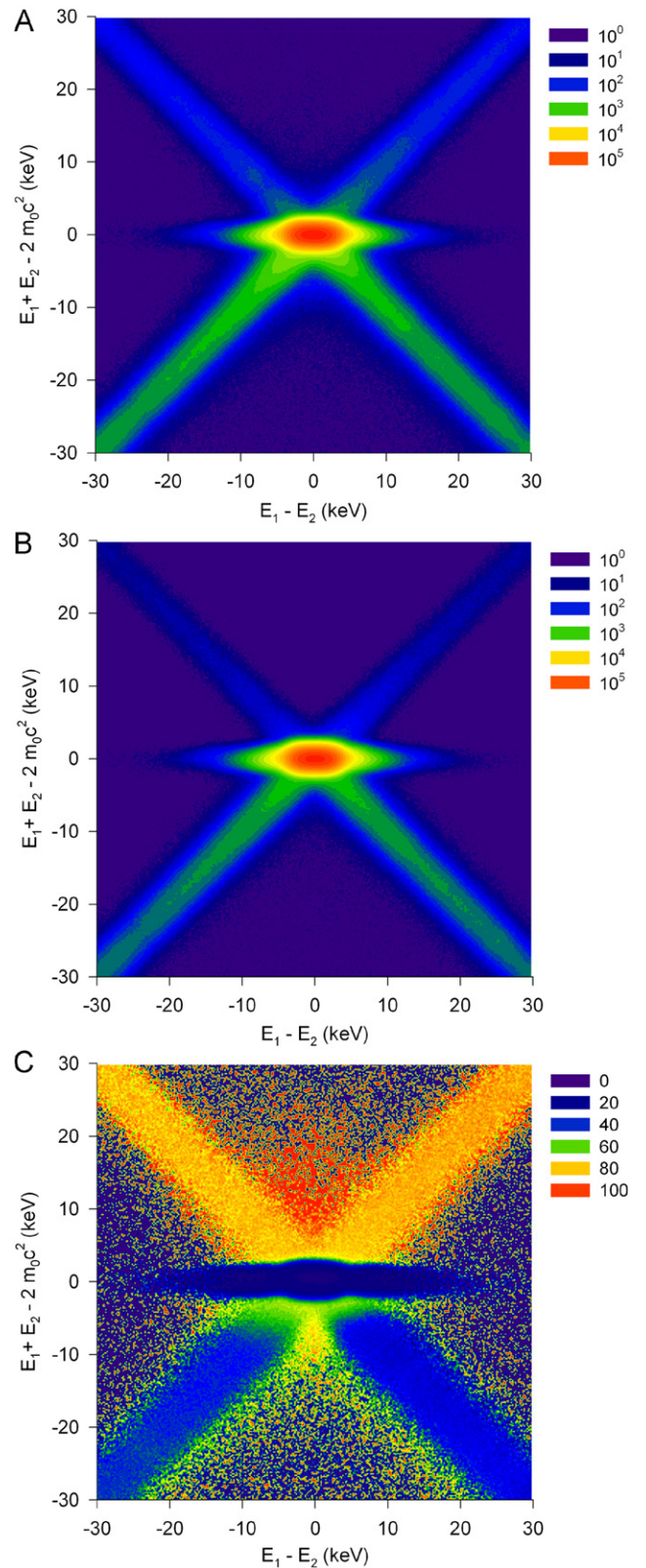


**Fig. 16.** Two-dimensional CDB spectra measured on reference pure Al sample in a semi-digital configuration. (A) The spectrum constructed from all waveforms which passed fixed filters, i.e. without application of shape filters. (B) The spectrum constructed only from waveforms which were accepted by shape filters. (C) The relative difference (in percents) between the CDB spectra (A) and (B).

that shape filtering rejects mainly pile-up events on the “wings” above the annihilation peak and makes the region around the annihilation peak cleaner by removing the events damaged by ballistic deficit. Hence, we can conclude that digital setup with shape filters enables to achieve CDB spectrum of improved clarity compared to traditional analogue setup.

### 3.3. Benchmark tests

The performance of digital CDB spectrometer in both semi-digital and pure-digital configurations was tested using well-annealed high purity Fe and Al reference samples. The experimental data were directly compared with *ab initio* theoretical calculations of high-momentum part (HMP) of momentum distribution of annihilating electron–positron pair. The HMP calculations were performed by atomic superposition (ATSUP)

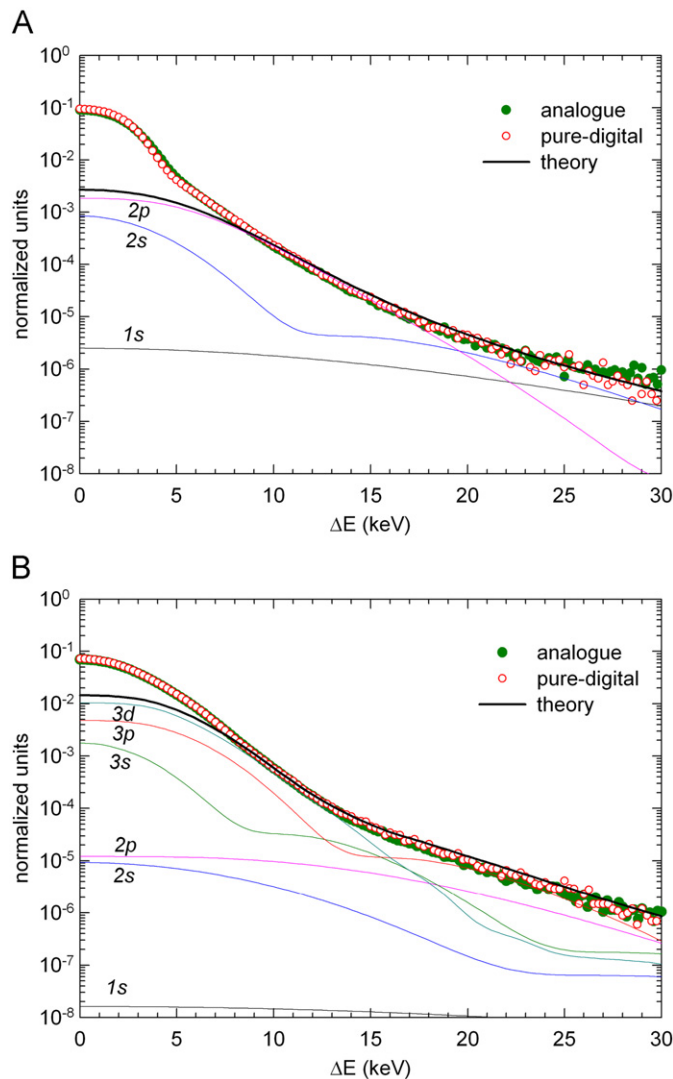


**Fig. 17.** Momentum distribution of annihilating electron–positron pairs (Doppler broadened profiles) measured on (A) pure Al reference specimen, (B) pure Fe reference specimen. Momentum distribution measured by analogue setup and pure-digital setup, respectively, are plotted by full and open points. Only the part of momentum distribution corresponding to positive Doppler shifts are plotted in the figure. Theoretical HMP curve calculated for Al and Fe is plotted by thick solid line. Thin solid lines show calculated partial contributions of individual core electron orbitals. Valence electrons were not considered in theoretical calculations, therefore, comparison of theoretical curve with experiment is meaningful only in the high momentum range  $\Delta E \geq 10$  keV where contribution of core electrons dominates.

technique within a scheme described in Refs. [19,20]. The electron–positron correlation effects were taken into account using the generalized gradient approximation (GGA) scheme introduced by Barbiellini et al. [21]. As valence electrons were not included in HMP calculations, comparison of theoretical HMP curves with experiment is meaningful only in high momentum range ( $\Delta E \geq 10$  keV) where contribution of core electrons dominates. The following configurations were used in HMP calculations:  $1s^2 2s^2 2p^6$  orbitals and  $1s^2 2s^2 2p^6 3s^2 3p^6 3d^6$  orbitals were considered as core electrons in Al and Fe, respectively. The contribution of 3d electrons in Fe was weighted by a factor of 0.5 to account for semi-core character d-orbitals. In order to model finite resolution of CDB spectrometer, the theoretical HMP curves were convoluted with a Gaussian function with FWHM of 1.0 keV.

Figs. 17A and B, respectively, show Doppler broadened profiles, i.e. momentum distribution of annihilating electron–positron pairs, measured on Al and Fe reference specimens. Note that only the part of symmetrical Doppler broadened profiles corresponding to positive Doppler shifts are plotted in Fig. 17. The theoretical HMP curves are plotted in Fig. 17 by solid lines together with partial contributions of core electron orbitals. One can see in the figures that CDB profile for Al exhibits a curved bell-shape maximum, while the profile for Fe exhibits broader maximum with less steep slope due to contribution of d electrons, which are absent in Al. Figs. 17A and B demonstrate that theoretical HMP curves exhibit a good agreement with experimental points in the high momentum range ( $\Delta E \geq 10$  keV), where contribution of positrons annihilated by core electrons dominates. Hence we can conclude that a satisfactory agreement between the experimental data measured on our CDB spectrometers and *ab initio* theoretical calculations was achieved.

To visualize even small differences between CDB profiles it is common to plot ratio curves of the CDB profile for the sample of interest divided by the CDB profile of a well defined reference [22]. Note that both CDB profiles are normalized to the same area. Here we used pure Al sample as reference and Fig. 18 shows the ratio curves for pure Fe (related to the Al reference). The main feature of the ratio curve is a peak located at  $\Delta E \approx 5.5$  keV which is caused by positrons annihilated by 3d Fe electrons. The solid line

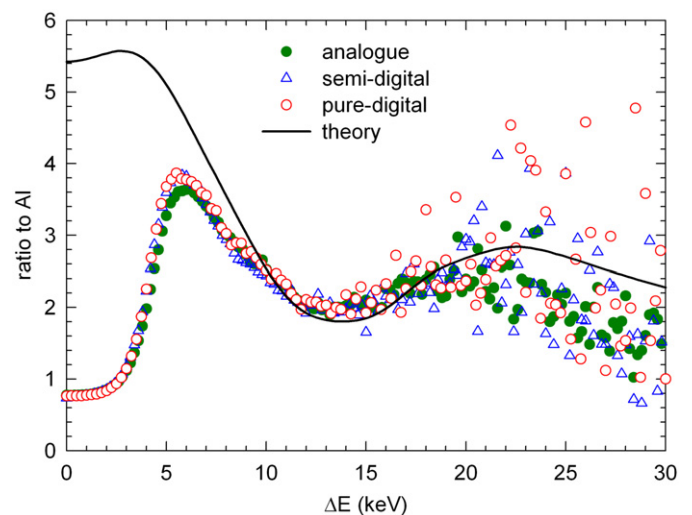


**Fig. 18.** Ratio curve (related to Al) for pure Fe reference specimen. Experimental curve obtained by using analogue (full circles), semi-digital (open triangles) and pure-digital (open-circles) is compared. Theoretical ratio curve obtained using the approach described in the text is plotted by a solid line. Valence electrons were not considered in theoretical calculations, therefore, comparison of theoretical curve with experiment is meaningful only in the high momentum range  $\Delta E \geq 10$  keV where contribution of core electrons dominates.

plotted in the figure is ratio curve constructed from the calculated HMP curves. Again we can conclude that there is a satisfactorily agreement between experimental points and theoretical ratio curve in the high momentum range  $\Delta E \geq 10$  keV.

### 3.4. Annihilation in flight

Significant suppression of background in coincidence measurement enables to detect annihilation in flight [23–27], i.e. extremely rare events when positron is annihilated during its slowing down process before its kinetic energy decreased down to thermal energy of  $\frac{3}{2}kT$ , where  $k$  is the Boltzmann constant and  $T$  is the thermodynamic temperature of the sample. Contrary to thermalized positron, momentum of *non-thermalized* “hot” positron is much higher than momentum of electron. Hence, assuming  $p_+ \gg p_-$  and neglecting the electron binding energy  $E_B$  Eq. (1) becomes

$$E_1 + E_2 = m_0c^2 + \sqrt{m_0^2c^4 + p_+^2c^2}. \quad (13)$$

The conservation of momentum simultaneously yields

$$E_1 - E_2 = cp_+. \quad (14)$$

Hence, combination of Eqs. (13) and (14) gives

$$E_1 + E_2 - 2m_0c^2 = \sqrt{(E_1 - E_2)^2 + m_0^2c^4} - m_0c^2. \quad (15)$$

Fig. 19 shows the two-dimensional CDB spectrum, i.e. histogram  $E_1 + E_2 - 2m_0c^2$  versus  $E_1 - E_2$ , measured on the reference Al sample using a semi-digital setup. Thus, the histogram plotted in Fig. 19 is identical with that plotted in Fig. 13B but now it is plotted in a significantly wider energy range. In Fig. 19 one can see clearly a hyperbolic feature which comes from positrons annihilating in flight. The solid line plotted in Fig. 19 is curve calculated using Eq. (15). Obviously, Eq. (15) describes well the shape of the contribution coming from annihilations in flight as was determined in experiment. It has to be mentioned that digital CDB spectrometer is very suitable for investigation of annihilation in flight due to digital shape filters which enable to reject distorted or damaged waveforms and to improve clarity of CDB spectrum as was demonstrated in Fig. 16.

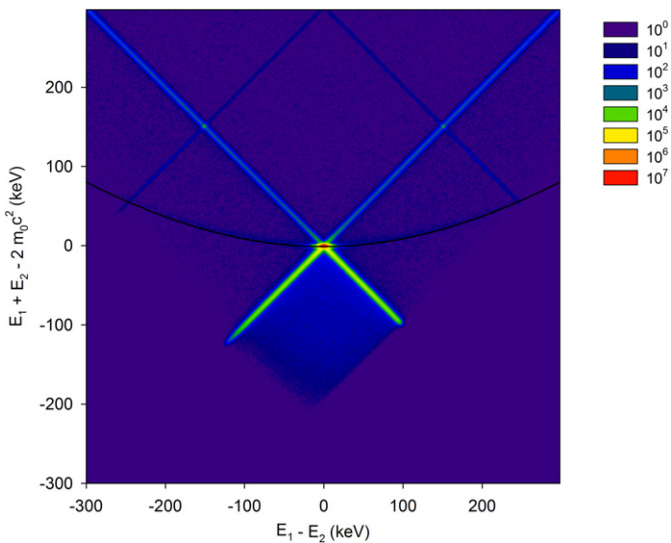


**Fig. 19.** Two-dimensional CDB spectrum measured on reference pure Al specimen by using a semi-digital setup. The spectrum is plotted in a wide energy range to show contribution of positrons annihilating in flight. The solid curve was calculated using Eq. (15).

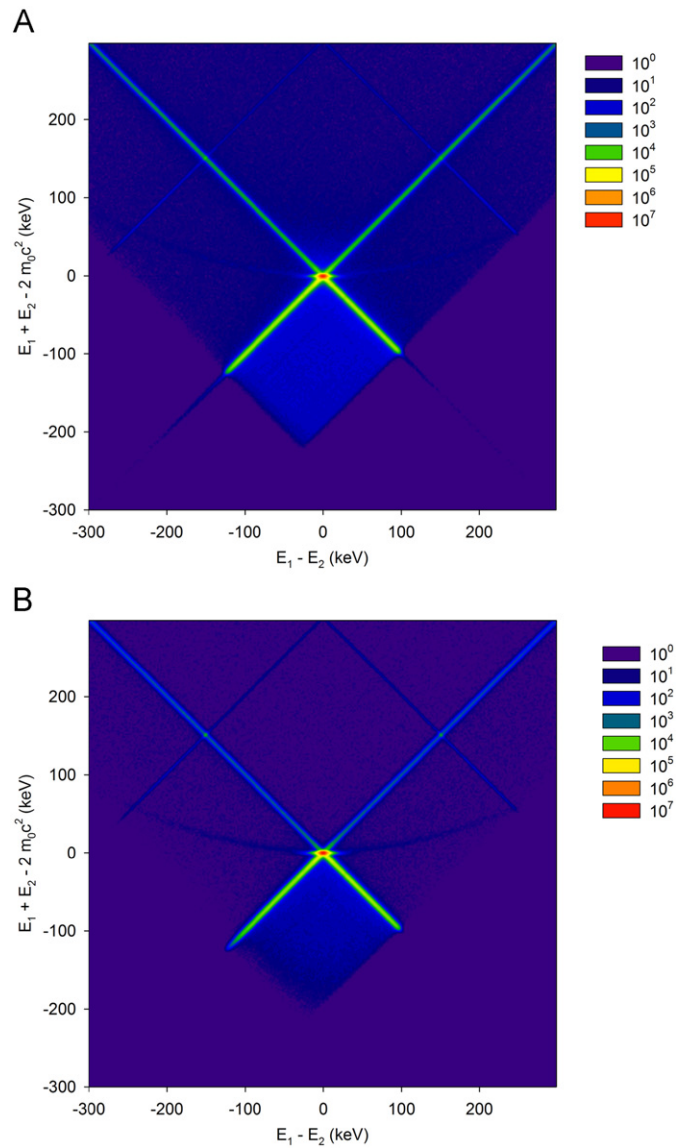


**Fig. 20.** Two-dimensional CDB spectrum measured on reference pure Al specimen by using a semi-digital setup plotted in a wide energy range to show contribution of positrons annihilating in flight. (A) Spectrum obtained without application of shape filters, (B) spectrum constructed only from waveforms which passed shape filters.

The importance of shape filtering in detection of annihilation in flight is illustrated in Fig. 20 which compares two-dimensional CDB spectrum obtained without application of shape filters (Fig. 20A) and spectrum constructed only from those waveforms which were accepted by shape filters (Fig. 20B). Comparison of Figs. 20A and B shows clearly that shape filters suppress undesired background from random coincidences but leave the contribution of positrons annihilating in flight unchanged. As a consequence the hyperbolic contribution of positrons annihilating in flight becomes much clearer visible in Fig. 20B obtained after application of shape filters.

## 4. Conclusions

The new digital CDB spectrometer described here is equipped with two high-purity Ge detectors and uses two-channel 12-bit digitizer for sampling of detector signals which are subsequently analyzed by a software procedure. The spectrometer can work in

two configurations called semi-digital and digital setup. In semi-digital setup detector signals are shaped prior to digitization into a pseudo-Gaussian shape by spectroscopy amplifier in order to improve signal-to-noise ratio. The maximum of the sampled waveforms is then determined by parabolic fitting. In the pure-digital configuration the detector signals are sampled directly. The acquired waveforms are subsequently fitted by a model function consisting of exponential decay function convoluted with Gaussian. Performance of the digital CDB spectrometer was compared with the traditional analogue setup connected to the same detectors. It was found that energy resolution achieved in a semi-digital setup is virtually the same as that in the analogue configuration. Superior energy resolution was achieved in pure-digital setup. Moreover, digital CDB spectrometer enables to obtain much better control over shape of detector signals. It was shown that damaged or distorted pulses can be very efficiently eliminated using digital shape filters. Hence, digital spectrometer enables to obtain CDB spectrum of superior clarity compared to its analogue counterpart. This was demonstrated by very efficient detection of a rare contribution of positrons annihilating in flight.

### Acknowledgment

This work was supported by The Ministry of Education, Youth, and Sports of The Czech Republic (Project no. MS 0021620834), The Academy of Science Czech Republic (Project no. KAN300100801) and The Czech Scientific Foundation (Project no. P108/10/0648).

### References

- [1] K.G. Lynn, J.R. MacDonald, R.A. Boie, L.C. Feldman, J.D. Gabbe, M.F. Robbins, E. Bonderup, J. Golovchenko, *Phys. Rev. Lett.* 38 (1977) 241.
- [2] M. Alatalo, H. Kauppinen, K. Saarinen, M.J. Puska, J.M. Akinen, P.H. Arvi, R.M. Nieminen, *Phys. Rev. B* 51 (1995) 4176.
- [3] P. Asoka-Kumar, M. Alatalo, V. Ghosh, A.C. Kruseman, B. Nielsen, K.G. Lynn, *Phys. Rev. Lett.* 77 (1996) 2097.
- [4] A. Somoza, M.P. Petkov, K.G. Lynn, A. Dupasquier, *Phys. Rev. B* 65 (2002) 094107.
- [5] M. Stadlbauer, C. Hugenschmidt, K. Schreckenbach, P. Böni, *Phys. Rev. B* 76 (2007) 174104.
- [6] Y. Nagai, M. Hasegawa, Z. Tang, A. Hempel, K. Yubuta, T. Shimamura, Y. Kawazoe, A. Kawai, F. Kano, *Phys. Rev. B* 61 (2000) 6574.
- [7] J. Čížek, O. Melikhova, I. Procházka, J. Kuriplach, I. Stulíková, P. Vostrý, J. Faltus, *Phys. Rev. B* 71 (2005) 064106.
- [8] H. Saito, Y. Nagashima, T. Kurihara, T. Hyodo, *Nucl. Instr. and Meth. A* 487 (2002) 612.
- [9] J. Nissilä, K. Rytsölä, R. Aavikko, A. Laakso, K. Saarinen, P. Hautojärvi, *Nucl. Instr. and Meth. A* 538 (2005) 778.
- [10] F. Bečvář, J. Čížek, I. Procházka, J. Janotová, *Nucl. Instr. and Meth. A* 539 (2005) 372.
- [11] F. Bečvář, J. Čížek, I. Procházka, *Acta Phys. Pol. A* 113 (2008) 1279.
- [12] F. Bečvář, J. Čížek, I. Procházka, *Appl. Surf. Sci.* 255 (2008) 111.
- [13] F. Bečvář, *Nucl. Instr. and Meth. B* 261 (2007) 871.
- [14] S.V. Petegem, B.V. Waeyenberge, D. Segers, C. Dauwe, *Nucl. Instr. and Meth. A* 513 (2003) 622.
- [15] Spectroscopy Amplifier Canberra Model 2020 Manual, [www.canberra.com](http://www.canberra.com).
- [16] W.R. Leo, *Techniques for Nuclear and Particle Physics Experiments*, Springer, Heidelberg, 1994.
- [17] U. Fano, *Phys. Rev.* 72 (1947) 26.
- [18] G.F. Knoll, *Radiation Detection and Measurement*, Wiley, New York, 2002.
- [19] M. Alatalo, B. Barbiellini, M. Hakala, H. Kauppinen, T. Korhonen, M.J. Puska, K. Saarinen, P. Hautojärvi, R.M. Nieminen, *Phys. Rev. B* 54 (1996) 2397.
- [20] J. Kuriplach, A.L. Morales, C. Dauwe, D. Segers, M. Šob, *Phys. Rev. B* 58 (1998) 10475.
- [21] B. Barbiellini, M.J. Puska, T. Korhonen, A. Harju, T. Torsti, R.M. Nieminen, *Phys. Rev. B* 53 (1996) 16201.
- [22] J. Gebauer, R. Krause-Rehberg, S. Eichler, F. Börner, *Appl. Surf. Sci.* 149 (1999) 110.
- [23] A.W. Hunt, M.H. Weber, J.A. Golovchenko, K.G. Lynn, *Appl. Surf. Sci.* 149 (1999) 282.
- [24] E. do Nascimento, O. Helene, C. Takiya, V.R. Vanin, *Nucl. Instr. and Meth. A* 538 (2005) 723.
- [25] E. do Nascimento, O. Helene, V.R. Vanin, M.T.F. da Cruz, *Nucl. Instr. and Meth. B* 247 (2006) 38.
- [26] J. Dryzek, T. Suzuki, R. Yu, *Radiat. Phys. Chem.* 76 (2007) 297.
- [27] E. do Nascimento, O. Helene, V.R. Vanin, M.T.F. da Cruz, M. Moralles, *Nucl. Instr. and Meth. A* 609 (2009) 244.